Available online at www.sciencedirect.com
ScienceDirect
Journal of Solid State Chemistry 180 (2007) 249–259
JOURNAL OF SOLID STATE CHEMISTRY
www.elsevier.com/locate/jssc

New misfit-layered cobalt oxide $(CaOH)_{1.14}CoO_2$

Mitsuyuki Shizuya, Masaaki Isobe*, Yuji Baba, Takuro Nagai, Minoru Osada, Kosuke Kosuda, Satoshi Takenouchi, Yoshio Matsui, Eiji Takayama-Muromachi

National Institute for Materials Science, 1-1 Namiki, Tsukuba, Ibaraki 305-0044, Japan

Received 28 April 2006; received in revised form 17 October 2006; accepted 17 October 2006
Available online 21 October 2006

Abstract

We synthesized a new cobalt oxide $(CaOH)_{1.14}CoO_2$ by utilizing a high-pressure technique. X-ray and electron diffraction studies revealed that the compound has a layered structure that consists of CdI_2-type CoO_2 layers and rock-salt-type double CaOH atomic layers. The two subcells have incommensurate periodicity along the *a*-axis, resulting in a misfit-layered structure. From resistivity and Seebeck coefficient measurements, we have shown that the two-dimensional (2-D) variable-range hopping (VRH) regime with hole conduction is dominant at low temperature for this compound. As temperature increases, the conduction mechanism undergoes crossover from the 2-D VRH regime to a thermal activation-energy-type regime.

Keywords: Layered cobalt oxide; Thermoelectric oxide; New-material design; Electron microscopy; Seebeck coefficient; Variable-range hopping

1. Introduction

Layered cobalt oxides have recently attracted much attention from solid-state physicists and chemists because of various unusual physical properties they possess. In particular, unconventional superconductivity found in $Na_{0.35}CoO_2 \cdot 1.3H_2O$ [1] greatly stimulates our intellectual curiosity, because the origin of the superconductivity seems to be associated with rather unusual spin-triplet-type electron pairing with ferromagnetic spin fluctuation [2]. Another most interesting characteristic feature is the large thermoelectric power realized in the layered cobalt oxides such as γ-$NaCo_2O_4$, [3] $Ca_3Co_4O_9$, [4], and $(Bi_2Sr_2O_4)_x CoO_2$. [5] These compounds have comparatively large Seebeck coefficients S in spite of their metallic resistivity ρ, resulting in large power factors S^2/ρ. In general, a large thermoelectric figure of merit Z $(= S^2/\rho\kappa$; κ, thermal conductivity) is an important factor from the viewpoint of application of compounds in high-performance thermoelectric devices. Moreover, many other interesting features, e.g., large magneto-resistance, [4,6,7] magnetic anomaly [8,9], and spin-density wave [10], have been observed in the layered cobalt oxides. These unusual physical properties seem to be caused by strong Coulomb interaction and collective excitation of electrons in a cobalt–oxygen hybridized narrow band. It is important for progress in solid-state physics to understand the origin of the quantum phenomena due to the strong electron correlation.

To understand the nature of the electron correlation in the layered cobalt oxides, it is important to find a new class of materials with more fascinating physical properties such as unconventional superconductivity. The search for new materials may lead to an improved understanding of the unusual physical properties and may ultimately lead to the discovery of novel functions in the materials. The layered cobalt oxides have common features in the crystal structure. The crystal structure consists of CdI_2-type conducting CoO_2 layers and insulating blocking layers. Accordingly, if we replace the blocking layers with any other types of structure while maintaining the CoO_2 layers, we can obtain a new class of material. This idea is similar to that for material design of the homologous series of high-T_c cuprate superconductors [11,12]. Thus far, many high-T_c cuprate superconductors with various structure types of blocking layers have been found based on a similar idea for

*Corresponding author. Fax: +81 29 860 4674.
E-mail address: ISOBE.Masaaki@nims.go.jp (M. Isobe).

0022-4596/$ - see front matter © 2006 Elsevier Inc. All rights reserved.
doi:10.1016/j.jssc.2006.10.014

material design, and the discovery of the new materials has greatly supported further understanding of physics and chemistry in high-T_c superconductivity. Our original idea in this study was to apply the same guiding principle for material design to search for a new phase for the layered cobalt oxides.

The layered cobalt oxides can be classified by the number of atomic layers, n, in the blocking layer. Fig. 1 shows a schematic representation of the crystal structures of a series of layered cobalt oxides. For instance, Na_xCoO_2 ($x = 0.3-0.7$) has a single atomic layer of sodium between the CoO_2 layers, and this can be regarded as the $n = 1$ member of the series. Other compounds, such as $[Ca_2CoO_3]_{0.62}CoO_2$ [4,13] and $[Bi_{0.87}SrO_2]_2[CoO_2]_{1.82}$ [14], have triple and quadruple atomic layers in the blocking layers with the rock-salt-type structure; that is, these are the $n = 3$ and 4 members of the series, respectively. However, only the double atomic-layer compound, the $n = 2$ member of the series, had not been reported until we completed the present study [15]. This was the "missing link" in the series of layered cobalt oxides. The aim of the present work was to prepare the $n = 2$ member of the series of layered cobalt oxides by the high-pressure synthesis technique, to complete the series. In general, high-pressure conditions are favorable for stabilizing the phases that include the closest-packed structure with the CoO_2 layer block. Indeed, we carried out phase search experiments under high pressure, and recently succeeded in synthesizing the intended compound having double atomic layers in the blocking layer.

In this paper, we report the crystal structure and physical properties of cobalt calcium hydroxide $(CaOH)_{1.14}CoO_2$. X-ray and electron diffraction (ED) studies revealed that this compound is a composite crystal that consists of two interpenetrated subsystems of CdI_2-type CoO_2 layers and the rock-salt-type double CaOH atomic layers. This structure is similar to that in the layered sulfides $(MS)_xTS_2$ (M = Sn, Pb, Bi or lanthanides; T = Nb, Ta, Ti, V, or Cr) [16–19]. We have shown that the present compound is electrically insulating due to insufficiency of doped carriers. The physical properties of the present compound originate in a "low-carrier-density limit" of the hole band, which is a rare case of electronic state for the series of CoO_2-layered structure system.

2. Experiment

A polycrystalline sample was prepared by means of a solid-state reaction using the high-pressure synthesis technique. The sample was made from a mixture of starting materials, Co_3O_4 (99.9%), CaO_2 (99%), CaO, and $Ca(OH)_2$ [20]. The reagents with a molar ratio of Co_3O_4:CaO_2:CaO:$Ca(OH)_2$ = 1:0.4952:1.2832:1.5732 were mixed using an agate mortar in a glove box filled with dry Ar gas [21]. The mixture was sealed into a gold capsule, and then allowed to react in a flat-belt-type high-pressure apparatus under 6 GPa at 1373–1473 K for 1 h, followed by quenching to room temperature before releasing the pressure.

The purity of the product was carefully checked by powder X-ray diffraction (XRD). We confirmed that the as-sintered product contained a small amount of $Ca(OH)_2$ as an impurity phase. To remove the $Ca(OH)_2$, some fractions of the product were roughly pulverized and washed with ion-exchanged water (200 mL per 200–300 mg sample powder) for 5 min using an ultrasonic cleaner. The wash process was repeated three times, replacing the water with clean water. After the wash, the powder was dried at 423 K in air. Hereafter, as-sintered bulk ceramics are called "bulk sample" or "as-grown sample", and wash powder is called "washed sample." The cation ratio of the high-pressure phase in the sample was determined by electron probe microanalysis (EPMA) using a wavelength-dispersive X-ray spectrometer (JEOL, JXA-8500F) with an acceleration voltage of 15 kV. In EPMA, a small ceramic specimen of the bulk sample was well polished using a 0.3-μm alumina lapping film to obtain a flat surface, and several relatively large grains were selected and analyzed. The average grain size of the phase was about $100 \times 30\,\mu m^2$.

Hydrogen content in the washed sample was determined by infrared (IR) absorption spectroscopic analysis with a carbon/hydrogen analyzer (LECO, RC-412). In the measurement, as temperature increases, hydrogen atoms in the sample react with oxygen atoms in the phase or carrier oxygen gas, and simultaneously yield H_2O vapor. The intensity of the IR-absorption spectrum due to the vaporized H_2O was recorded during the heating. The amount of H_2O in the sample was determined by calibrating the intensity data using $Na_2WO_4 \cdot 2H_2O$ as standard material. To avoid detecting the water adhering onto grain surfaces and/or boundaries, the samples were pre-heated at 423 K before the measurement.

The content of cobalt atoms in the washed sample was determined by inductively coupled plasma atomic emission spectrometry, after dissolving the sample powder in hydrochloric acid. The oxidation state of the cobalt ion was determined by redox titration. The washed sample was dissolved in sulfuric acid containing an excess of sodium oxalate $(COONa)_2$ as reducing agent. The residual $(COONa)_2$ was titrated against an aqueous solution of potassium permanganate ($KMnO_4$) to reduce the oxidation state of the cobalt ions.

Powder XRD data were collected at room temperature using a diffractometer (Rigaku, RINT2200HF-ULTIMA) equipped with Bragg–Brentano geometry and Cu$K\alpha$ radiation. Lattice constants were determined by the least-squares method. The crystal structure was analyzed by computer simulation of the XRD pattern using PRE-MOS91 software on the basis of the superspace group symmetry approach [22]. Transmission electron microscopy (TEM) observations were carried out using a microscope (Hitachi, H-1500) operating at 820 kV. The bulk sample was pulverized in an agate mortar, and the powder was dispersed in CCl_4 using an ultrasonic cleaner.

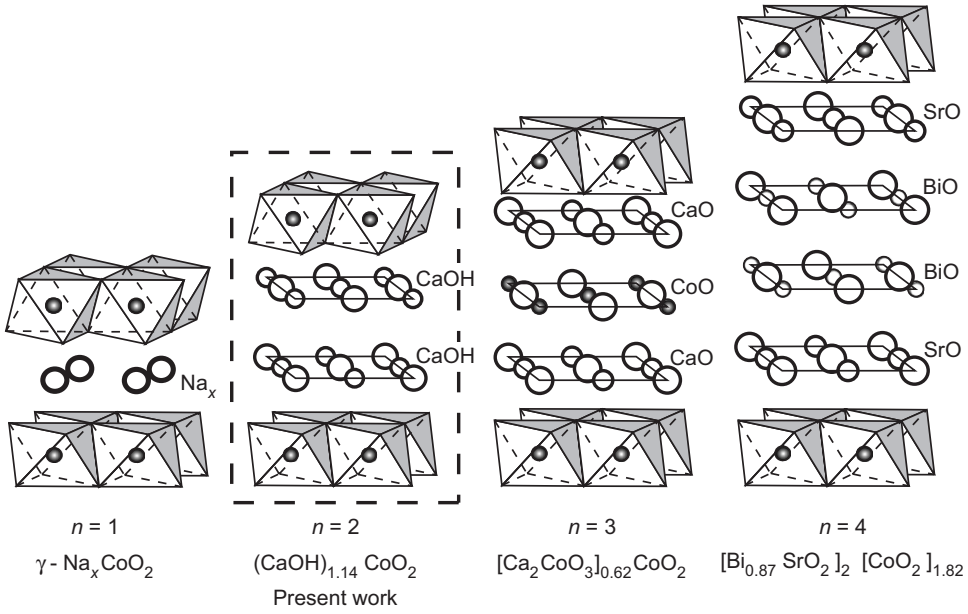

Fig. 1. Schematic representation of the crystal structure of the layered cobalt oxides: n indicates the number of atomic planes in the blocking layer situated between the CoO_2 layers. The $n = 2$ compound, $(CaOH)_{1.14}CoO_2$, is a new member of the series reported in the present work.

The supernatant fluid containing fine powder was collected and dropped onto carbon micro-grids for observation.

Raman experiments were carried out in a backward micro-configuration to study the bonding state of hydrogen in the phase. An Ar^+ laser (1 mW, 514.5 nm line) beam with a 2-μm diameter spot was focused on individual grains in the washed sample at room temperature. The scattered light was recorded using a subtractive triple liquid N_2-cooled spectrometer (T64000, HORIBA Jobin-Yvon) equipped with a charge-coupled device detector.

Magnetic data were collected for the pulverized sample using a superconducting quantum interference device magnetometer (Quantum Design, MPMS) on cooling in a magnetic field of 1000 Oe from 2 to 300 K.

The Seebeck coefficient was measured by a thermal transport option using a commercial apparatus (Quantum Design, PPMS) with a four-probe configuration. The sample size was $1.4 \times 2.0 \times 5.3\,mm^3$, and the distance between the two temperature/voltage terminals was 2.3 mm. Copper wires were attached onto the polished sample surface via evaporated thin gold film using silver paste in order to make fine Ohmic contact. Data were collected using continuous mode at a cooling rate of 0.3 K/min. Temperatures at the two temperature/voltage terminals were detected by thermometers (Cernox 1050), and the temperature difference between the two terminals was controlled within 3% of the measurement temperature. Electrical resistivity was measured by the conventional four-probe AC method simultaneously with the thermoelectric power measurement. An AC of 0.5–0.01 mA with 60–300 Hz was applied to the sample.

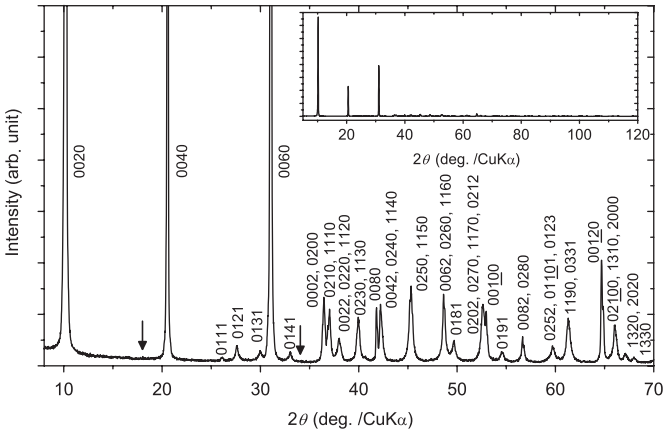

Fig. 2. Powder X-ray diffraction patterns for the washed-sample of $(CaOH)_{1.14}CoO_2$; the inset is a whole 2θ range pattern, while the main panel is an enlargement of the pattern. The arrows in the main panel indicate no trace of the unreacted impurity phase, $Ca(OH)_2$.

3. Results and discussion

3.1. Characterization

Fig. 2 shows XRD patterns for the washed sample; the inset shows a whole 2θ range pattern, while the main panel shows the enlarged pattern. We confirmed that the washed sample does not contain any trace of the $Ca(OH)_2$ impurity phase as shown by arrows in the main panel of Fig. 2. This indicates that the $Ca(OH)_2$ phase was entirely removed from the sample by the water-wash process. No other differences were observed in the XRD patterns before and

after the wash process, suggesting that the main phase does not react with water.

The intensities of the reflections with d-values of $\approx 8.7 \times 1/n$ Å (n: integer), including three intense reflections in the low 2θ angle range, are enhanced owing to a strong preferred orientation. The intensities in the higher angle range ($n \geqslant 4$) seem rather weak. Using powder XRD simulation discussed later (Fig. 7), we confirmed that they are also enhanced. This suggests that the present phase has a layer structure with a periodicity of $d \approx 8.7$ Å along the direction perpendicular to the layer, and that the crystal grain easily cleaves into many plate-like crystals during X-ray sample preparation.

In Fig. 2, all diffraction peaks can be systematically indexed by sets of four integers, $hklm$, by assuming that the present phase is a composite crystal having a (3 + 1)-dimensional structure. There are two c-centered orthorhombic subsystems with common b (= 4.9228(4) Å) and c (= 17.275(1) Å), and different a: $a_1 = 2.8238(2)$ Å for subsystem-1 and $a_2 = 4.944(2)$ Å for subsystem-2. The a_1, a_2, and b parameters are near to the lattice constants of other misfit-layered cobalt oxides, e.g., $a_1 = 2.8238(2)$ Å, $a_2 = 4.5582(2)$ Å, $b = 4.8339(3)$ Å for $[Ca_2CoO_3]_{0.62}CoO_2$ [13] and $a_1 = 2.8081(5)$ Å, $a_2 = 5.112(1)$ Å, $b = 4.904(1)$ Å for $[Bi_{0.87}SrO_2]_2[CoO_2]_{1.82}$ [14]. This suggests that the intralayer structure in the present compound is similar to those of the reference compounds. For subsystem-1, b is nearly equal to $\sqrt{3}a_1$, and the unit cell has a c-centered Bravais lattice. The lattice points form an approximately equilateral triangle lattice with hexagonal symmetry in the a–b plane. This indicates that subsystem-1 consists of CoO_2 layers with CdI_2-type structure. For subsystem-2, a_2 is nearly equal to b, suggesting that the unit lattice has approximately tetragonal symmetry. These parameters, a_2 and b, are close to twice the Ca–O distance 2.4 Å estimated by Shannon's ionic radii—1.0 Å for Ca^{2+} (6-fold coordination) and 1.4 Å for O^{2} (6-fold coordination) [23]. This indicates that subsystem-2 consists of CaO blocks with rock-salt-type structure.

The $c/2$ value is 8.638 Å, which corresponds to the nearest-neighbor distance between the CoO_2 layers. This length is comparable with the c parameters of $[Ca_2CoO_3]_{0.62}CoO_2$ ($c = 10.8436(7)$ Å) [13]. The difference in these values is due to the different number of stacking layers in the rock-salt-type structure block. $[Ca_2CoO_3]_{0.62}CoO_2$ has triple layers, [CaO]–[CoO]–[CaO], intervening between two CoO_2 layers along the c-axis. The difference in the $[CoO_2]$ inter-layer distances between the present compound and $[Ca_2CoO_3]_{0.62}CoO_2$ is 2.206 Å, which is relatively close to the [CoO] mono-layer thickness of 1.945 Å estimated using Shannon's ionic radii: 0.545 Å for Co^{3+} (6-fold coordination, low-spin state) and 1.4 Å for O^{2} (6-fold coordination) [23]. This suggests that the present compound has double [CaO] layers for the rock-salt-type structure block.

Along the a-axis, a_1/a_2 (= 0.5711(4)) is the ratio of incommensurate periodicity between the $[CoO_2]$ layer and [CaO] block. Twice this value corresponds to the Ca/Co ratio in the present compound. The actual Ca/Co cation ratio determined by EPMA was 1.14, which is consistent with the value estimated from the structural study.

From the XRD study, the composition of the present compound is expected to be $[Ca_2O_2]_{0.57}[CoO_2]$, namely $(CaO)_{1.14}CoO_2$, if we do not consider the hydrogen atoms. However, this is not exact, and we have to take into account the presence of hydrogen atoms for the actual composition. We measured the actual amount of hydrogen in the present phase by IR-absorption spectroscopic analysis. The resultant total amount of H_2O vaporized was 6.9 wt%, which corresponds to 1.2 hydrogen atoms per $(CaO)_{1.14}CoO_2$. This value is very close to the amount of oxygen atoms 1.14 in the CaO block, suggesting that almost all the hydrogen atoms are situated in the CaO block. We conceive that the hydrogen atoms bond with the oxygen atoms in the CaO block, yielding OH ions. The oxidation state of the cobalt ion determined by redox titration was +2.9 [24]. This value is consistent with the ideal cobalt valence of +2.86 estimated from the composition $(CaOH)_{1.14}CoO_2$, where we assumed the charge neutrality and the cation valences: Ca^{2+}, OH^{-}, and O^{2-}. Therefore, we concluded that the phase composition $(CaOH)_{1.14}CoO_2$ is more or less correct.

We observed the misfit-layered structure by TEM. Fig. 3(a)–(c) shows ED patterns projected along the [001], [010], and [100] directions, respectively. Fig. 3(a) is a typical ED pattern on the a^*–b^* section, which was frequently observed because a fraction of the crystal easily cleaves along the a–b plane. This pattern is essentially identical to those observed in other misfit-layered cobalt oxides such as $[Ca_2CoO_3]_{0.62}CoO_2$ [13] and $[Bi_{0.87}SrO_2]_2[CoO_2]_{1.82}$ [14]. In Fig. 3, fundamental reciprocal-lattice vectors of the two subsystems are shown by arrows. All the reflections, both the main and satellite reflections, can be assigned to a linear combination of four unit vectors, a_1^*, b^*, c^*, a_2^*, and four integers, $hklm$, with a reciprocal-lattice vector, q ($d = 1/|q|$), given by $\boldsymbol{q} = h\boldsymbol{a}_1^* + k\boldsymbol{b}^* + l\boldsymbol{c}^* + m\boldsymbol{a}_2^*$. The a_2^*/a_1^* value obtained is about 0.57, which is consistent with the a_1/a_2 (= 0.5711(4)) value obtained from the XRD study.

Fig. 4 shows a high-resolution transmission electron microscopy (HRTEM) image projected along the direction perpendicular to the c-axis. This clearly indicates layer stacking along the c-axis in a structure with double CaOH atomic layers sandwiched by two CoO_2 layers. The distance between the nearest-neighbor CoO_2 layers is about 8.7 Å, which is in agreement with the $c/2$ value (= 8.638 Å) obtained from the XRD study.

Reflection conditions observed in ED patterns are as follows: $h + k = 2n$ for $hk0$; $k + m = 2n$ for $0k0m$; h, $l = 2n$ for $h0l0$; l, $m = 2n$ for $00lm$; and $k = 2n$ for $0kl0$. The extinction indicates that the two subsystems have c-centered orthorhombic lattice symmetry. Possible space groups of the average structure are $Cmcm$ (no. 63), $Cmc2_1$ (no. 36), and $C2cm$ (no. 40) for subsystem-1, and $Cmc2_1$

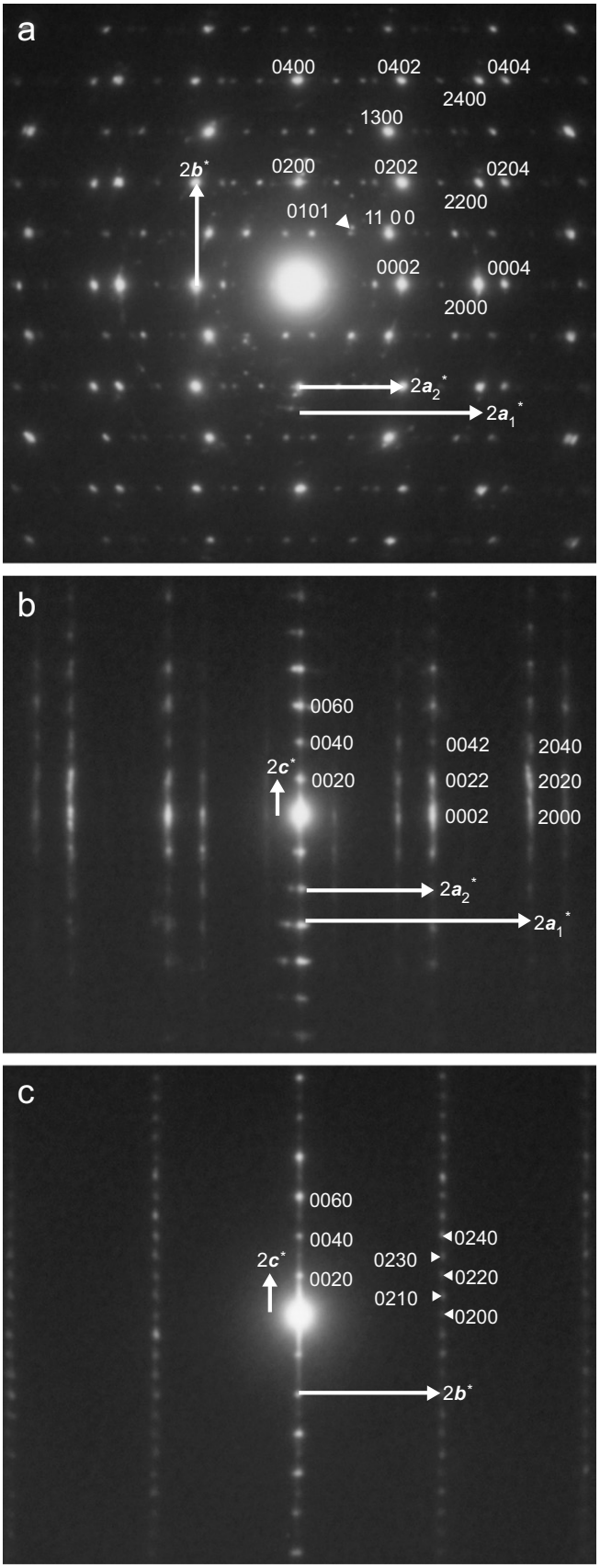

Fig. 3. Electron diffraction (ED) patterns projected along the [001] (a), [010] (b), and [100] (c) directions for $(CaOH)_{1.14}CoO_2$.

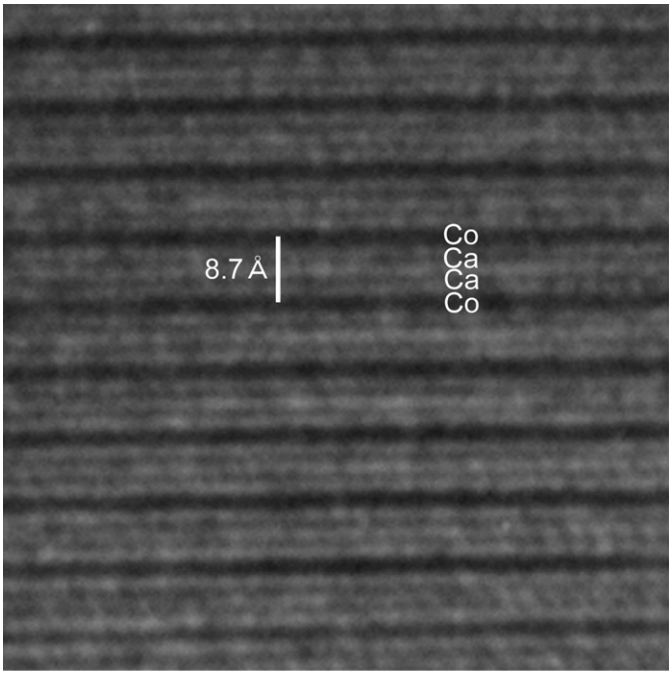

Fig. 4. High-resolution transmission electron microscopy (HRTEM) image projected along the direction perpendicular to the *c*-axis for $(CaOH)_{1.14}CoO_2$.

(no. 36) for subsystem-2 [25]. Note that the space groups *Cmcm* (no. 63) and *C*2*cm* (no. 40) cannot generate any rock-salt-type structures for subsystem-2.

Fig. 5 shows a possible structural model for $(CaOH)_{1.14}CoO_2$. In this structure, we employed symmetry with the non-centrosymmetric space group $Cmc2_1$ for both the subsystems. This structure is close to that observed in an orthorhombic phase of $(PbS)_{1.18}TiS_2$, except for the symmetry; $(PbS)_{1.18}TiS_2$ has a higher symmetry represented by a space group *Cmca* (no. 64) for both the subsystems [19]. All the proposed space groups indicate that the CoO_2 layers stack in a manner as shown schematically in Fig. 6(a). The structure in Fig. 6(a) has anti-parallel CoO_2 layers stacking along the *c*-axis; as a result, the lattice becomes orthorhombic with two CoO_2 layers in a unit cell. This situation has also been observed in $Ca_3Co_4O_9$ [26]. However, most of the misfit-layered cobalt oxides have a monoclinic lattice with parallel CoO_2 layers as shown in Fig. 6(b). Such a monoclinic lattice may also be realized for the present compound. The ED pattern of Fig. 3(c) has some bright spots overlapping with the $k \neq 0$ reflections (e.g., 0 2 7 0, 0 2 9 0, $0\bar{2}50$, and $0\bar{2}70$). These spots and 0 0 *l* 0 reflections form a reciprocal lattice corresponding to a monoclinic lattice with a lattice parameter $c/2$ and $\beta \approx 97^\circ$. However, the powder XRD pattern shown in Fig. 2 has no reflections indicating the existence of the monoclinic lattice, and all reflections observed can be indexed by the orthorhombic one. We conclude that the average stacking structure of the sample is orthorhombic, while the monoclinic lattice may also exist as a minor phase in the sample or as a stacking fault that we described in Fig. 6(c).

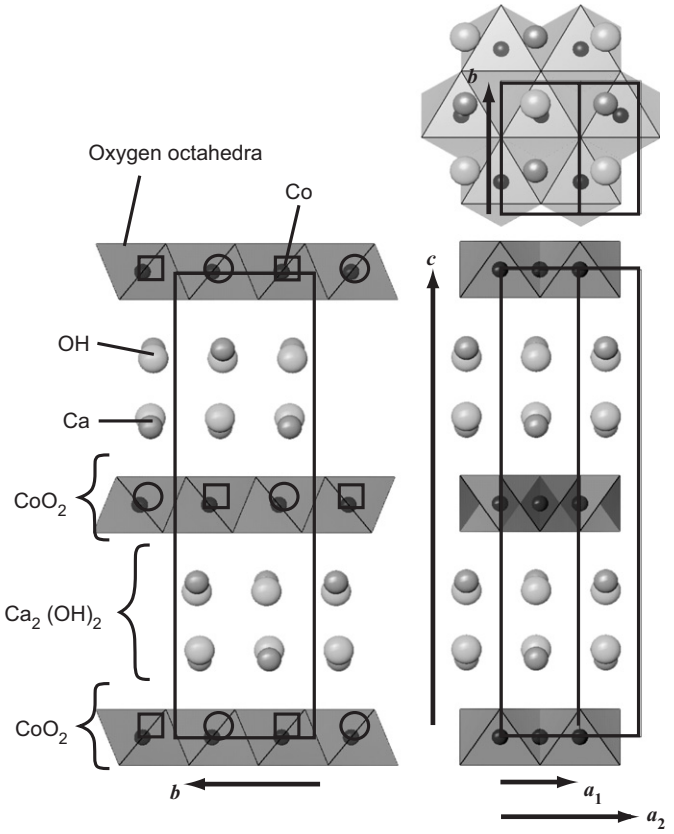

Fig. 5. Possible crystal-structure model of $(CaOH)_{1.14}CoO_2$. The rectangles indicate unit cells of the two subsystems. The open circles and squares represent the cobalt atoms situated at different positions along the projected coordinate. This drawing is idealized as if its structure was not modulated at all. (A part of this figure was drawn with a computer software VENUS developed by R.A. Dilanian and F. Izumi.)

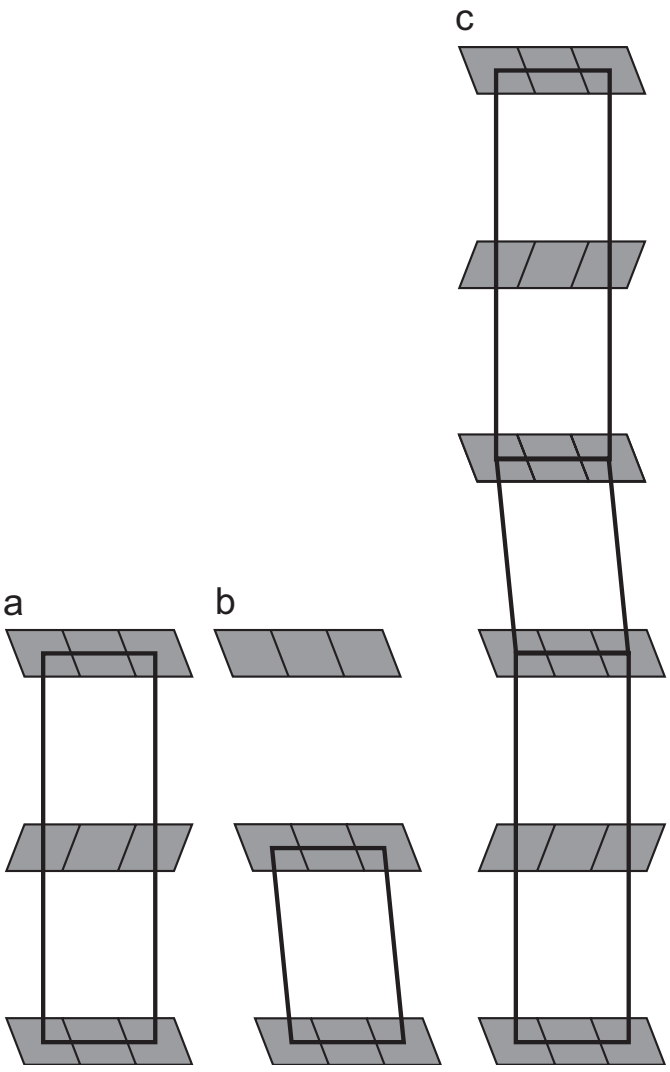

Fig. 6. Possible stacking patterns of CoO_2 layers for the misfit-layered cobalt oxides. Shaded areas represent CoO_2 layers where each diamond indicates CoO_6 octahedra. Solid rectangles are the unit cells. (a) Orthorhombic-type stacking, (b) monoclinic-type stacking and (c) orthorhombic-type stacking with a monoclinic stacking fault.

In the composite crystal, each substructure is modulated owing to the interaction between the subsystems. A four-dimensional structural analysis technique is necessary to determine the conclusive superspace group and details of the modulated structure realized in this compound. In the present study, in advance of the precise analysis of the modulated crystal structure, we simulated the XRD pattern using the PREMOS91 computer program. Fig. 7 shows an XRD pattern simulated on the basis of the crystal structure model proposed in Fig. 5. The calculated diffraction pattern is very similar to the observed one [27], indicating that the proposed crystal structural model is close to the actual crystal structure. We also considered another structural model with a higher symmetry based on the space group *Cmcm* (no. 63) for subsystem-1 and *Cmca* (no. 64) for subsystem-2. However, the simulation using this model could not accurately reproduce the observed XRD pattern.

In the above simulation based on the space group $Cmc2_1$, we found that the atomic configuration at which the best result was obtained is close to that of a structure having a higher symmetry with a space group *Cmca* (no. 64) for both the subsystems. This symmetry is equal to that of the orthorhombic phase $(PbS)_{1.18}TiS_2$ reported in Ref. [19]. If the actual symmetries for both the subsystems are represented by *Cmca*, the reflection spots with $h, k \neq 2n$ for $hk00$ (and $k, m \neq 2n$ for $0k0m$) should not appear in the ED pattern by the extinction rule, while they are observed in Fig. 3(a) (e.g., 1100). However, these reflections can also arise from the monoclinic stacking fault described in Fig. 6(c) if it exists in the present phase. In this case, it is possible that both the subsystems for the average crystal structure have orthorhombic symmetry with the space group *Cmca*, while the monoclinic stacking fault also exists in the microscopic structure.

From the chemical composition, it is most likely that hydrogen atoms exist in the rock-salt-type structure block as OH^- ions. We studied the bonding state between the oxygen and hydrogen atoms by Raman scattering experiments. Fig. 8 shows a Raman spectrum for the washed

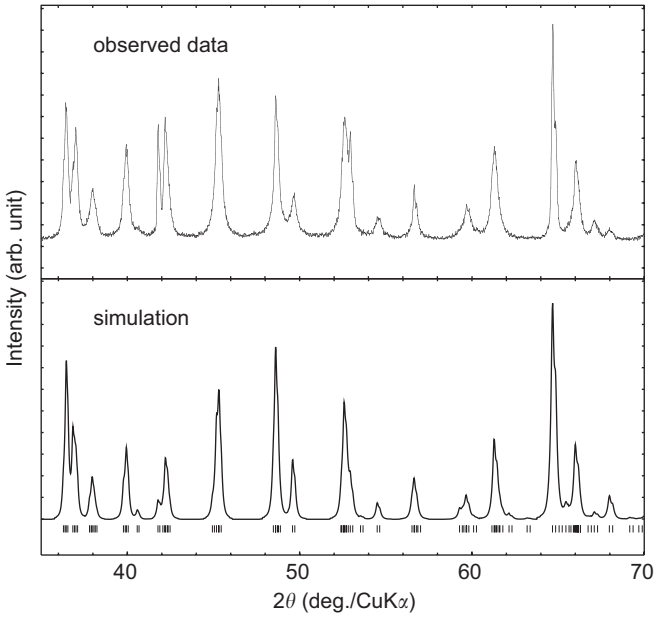

Fig. 7. X-ray diffraction pattern simulated on the basis of the proposed crystal structure model for $(CaOH)_{1.14}CoO_2$. The short vertical bars under the simulation pattern indicate positions of Bragg reflections. For comparison, the observed XRD pattern is also displayed in the upper panel of the figure.

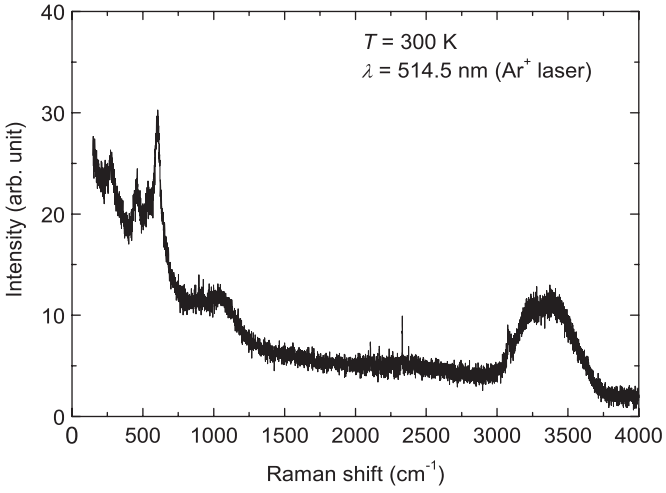

Fig. 8. Raman scattering spectrum for a crystalline grain in the washed-sample for $(CaOH)_{1.14}CoO_2$.

sample. The peaks with wavenumbers below 800 cm^{-1} are attributed to lattice vibration of ions, while the hump between 800 and 1500 cm^{-1} is due to the second harmonic generation of the lattice vibration. The peaks with wavenumbers above 2500 cm^{-1} are related to molecular vibration of the –OH groups. A broad intense peak was observed in the wavenumber range between 3000 and 3700 cm^{-1}. This peak is due to O–H stretching vibration mode in the –OH groups. No peak was observed around 1600 cm^{-1}. This indicates that the OH^- ions are dominant for the hydrogen–oxygen bonding state in the present compounds, because the other possible bonding states, e.g., H_2O molecule and H_3O^-, should cause Raman scattering peaks around 1600 cm^{-1} if they are included in this phase [28].

The broad peak has a maximum at 3230–3380 cm^{-1}. These frequencies are very low and the peak width is very broad compared with the typical peak frequency $\nu_{O-H} \approx 3600\,cm^{-1}$ and peak width $\Delta \approx 10\,cm^{-1}$ for general hydroxides such as $Co(OH)_2$ [29]. The frequency shift indicates that the O–H binding energy in the OH^- ions is weakened by interaction between hydrogen and other ions. This interaction probably arises from hydrogen bonding between the hydrogen and oxygen ions in the CoO_2 layer. This implies that the hydrogen atoms in the OH^- ions are directed toward the nearest-neighbor oxygen ion in the CoO_2 layers. The peak broadening seems to be related to the structural incommensurability between the two subsystems. The inter-atomic distance between the OH^- ion and the nearest-neighbor oxygen ion in the CoO_2 layer, i.e., hydrogen-bonding distance, markedly varies depending on each site position in the structure. The strength of the OH^- binding energy is affected by the structural modulation through the change in the hydrogen-bonding distance. As a result, various strengths of the OH^- binding energy exist in the entire crystal. This effect may cause peak broadening of the O–H molecular vibration.

A small sharp peak that overlaps with the broad peak was observed at 3077 cm^{-1}. This peak position is very close to the Raman scattering frequency due to H_3O^- ions, which was observed in the BLH phase of $Na_xCoO_2 \cdot yH_2O$ [30]. However, this peak is negligibly small compared with the integral intensity of the broad peak assigned to the OH^- ion. We conclude that this sharp peak is extrinsic to the present phase.

3.2. Physical properties

Fig. 9(a) shows the temperature dependence of the electrical resistivity of $(CaOH)_{1.14}CoO_2$. Thermally activated behavior was observed over the temperature range measured. The resistivity at room temperature is approximately 30 Ω cm, which is still $\sim 10^3$ times larger than that of the typical misfit-layered oxides, e.g., $Ca_3Co_4O_9$ [4]. The resistivity change looks to be semiconductor-like behavior; however, it does not maintain a simple activation-energy-type mechanism through the temperature range. We have shown that the resistivity below 270 K obeys the variable-range hopping (VRH) regime with the following formula: [31]

$$\rho(T) = \rho_0 \exp\left(\frac{T_0}{T}\right)^{\nu}, \quad (1)$$

where the exponent ν is a fractional value between 1/4 and 1, and depends on the dimensionality, electronic-band structure near the Fermi energy level (E_F), and Coulomb correlations between electrons [31–33].

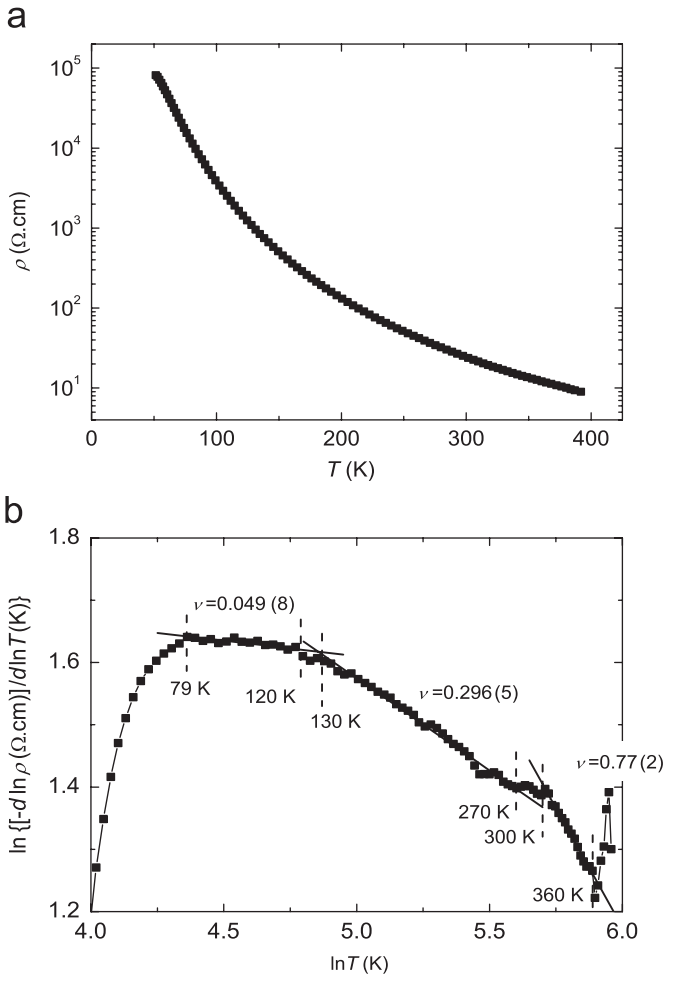

Fig. 9. Temperature dependence of electrical resistivity of $(CaOH)_{1.14}CoO_2$: (a) linear-logarithm plot and (b) logarithmic-derivative plot. Solid lines in (b) are results of linear fitting in three temperature ranges between temperatures specified by broken lines. The slopes of the solid lines give v in Eq. (1) (the numbers in parentheses are standard deviations of the fitting results).

To determine accurate v values for the present compound, we analyzed the resistivity data using the following formula derived from Eq. (1):

$$\ln\left(-\frac{\partial \ln \rho}{\partial \ln T}\right) = (\ln v + v \ln T_0) - v \ln T \quad (v \neq 0). \qquad (2)$$

In Fig. 9(b), we plotted $\ln[-\partial(\ln \rho)/\partial(\ln T)]$ vs. $\ln T$, where the slope of the fit gives $-v$. Three temperature ranges with different v are clearly defined: (i) $v = 0.049(8)$ for 79–120 K, (ii) $v = 0.296(5)$ for 130–270 K, and (iii) $v = 0.77(2)$ for 300–360 K [34]. In the temperature range of 130–270 K, the resistivity is well described by Eq. (1) with $v = 0.296$. This v value is approximately 1/3 which is the same value expected in the case of two-dimensional (2-D) VRH conduction [31]. We therefore concluded that the 2-D VRH regime is essentially dominant in this temperature range. The 2-D VRH regime observed in the temperature range probably originates from Anderson localization, which is caused by potential randomness due to local inhomogeneity of chemical composition or structural modulation in the CoO_2 layers. This suggests that the compound has a finite density of states $N(E)$ at the Fermi energy level E_F and the carriers around E_F are localized owing to the potential randomness. This implies that the electronic structure in the ground state is qualitatively nearer to what is expected in metals and not in semiconductors.

As the temperature increases, the slope v varies from 0.296 to 0.77 in a narrow temperature range of 270–300 K. This suggests the occurrence of a thermally induced crossover of the conduction mechanism. Above 300 K, the v value approaches 1, suggesting that the conductivity is associated with the activation-energy-type conduction mechanism. The activation energy ΔE was estimated to be about 0.1 eV by fitting the resistivity data in the temperature range with the conventional formula, $\rho(T) = \rho_0 \exp(\Delta E/k_B T)$. We conclude that the ΔE value corresponds to the energy for thermal excitation of carriers from E_F to a mobility edge in the conduction or valence band.

Below 130 K, the resistivity gradually strays from the 2-D VRH regime with decrease in temperature. In the temperature range of 80–120 K, the slope v is kept near zero, where the resistivity approximately follows the formula $\rho(T) = \rho_0 T^{-\alpha}$. Similar behavior is sometimes observed in polycrystalline samples of other transition-metal oxides; however, the origin of such a conduction mechanism is not clear at least in the present compound. Perhaps, this may be related to generation of tunnel current between the CoO_2 layers or the effect of grain-boundary scattering in the polycrystalline sample.

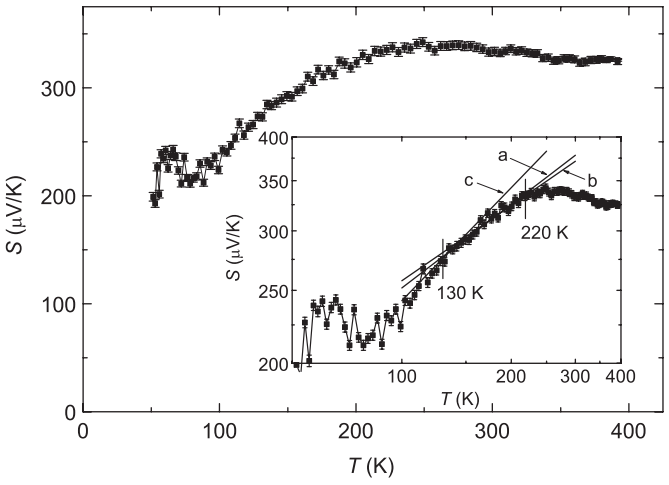

Fig. 10. Seebeck coefficient S of $(CaOH)_{1.14}CoO_2$ plotted as a function of temperature T. The inset shows a part of the enlarged logarithm–logarithm plot of the data. Error bars are the standard deviations in the experimental data. The solid line (a) in the inset shows a result of liner fitting between $130\,K < T < 220\,K$, where the result is $S = (46 \pm 4) \times T^{0.37 \pm 0.02}\,\mu V/K$. For comparison, $T^{1/3}$- and $T^{1/2}$-dependence of S are also shown by the solid lines (b) and (c), respectively.

The 2-D VRH regime was also observed in the thermoelectric power of this compound. Fig. 10 shows the temperature dependence of the Seebeck coefficient S of $(CaOH)_{1.14}CoO_2$. S has a positive sign through the whole temperature range measured, indicating that the majority carrier type is the hole. The absolute value of S at room temperature is about 330 μV/K, which is as large as those of typical band-gap semiconductors such as Si [35]. However, the observed temperature dependence is not typical semiconductor-like ($S \propto 1/T$) throughout the temperature range, but rather metal-like ($S \propto T$) at low temperature. It has been theoretically and experimentally confirmed that the metallic behavior of S occurs in the case of the VRH regime [36–39]. According to Mott et al. [31], the Seebeck coefficient S in the VRH regime is written as

$$S(T) = \frac{1}{2}\frac{k_B}{e}\frac{W^2}{k_B T}\left(\frac{\partial \ln N(E)}{\partial E}\right)_{E=E_F}, \quad (3)$$

where k_B is the Boltzmann constant, e is the unit charge of electrons, and W is the hopping energy. Brenig et al. [39] defined the hopping energy in the case of the 2-D VRH regime as follows:

$$W = \frac{1}{3} k_B T \left(\frac{T_0}{T}\right)^{1/3}. \quad (4)$$

Substituting Eq. (4) into Eq. (3), we can obtain the form $S \propto T^{1/3}$ in the case of the 2-D VRH regime. Similarly, $S \propto T^{1/2}$ dependence can be obtained for the 3-D VRH case [31,36–38]. In the present compound, a power law can be observed for $130\,K < T < 220\,K$ as shown in the inset of Fig. 10. By a linear fitting of this plot, we obtained $S \propto T^{0.37\pm0.02}$ dependence, which is close to the predicted dependence of the 2-D VRH case. The temperature range determined by the thermoelectric power measurement (130–220 K) is nearly equal to that by the resistivity measurement (130–270 K).

Above 220 K, the temperature dependence of the thermoelectric power strays out of the 2-D VRH conduction. The S value reaches a maximum at about 250 K, and then decreases with increasing temperature above 250 K. This suggests that, at 250 K, the dominant electronic transport mechanism changes from the 2-D VRH regime to thermal-activation-type band conduction by carrier excitation with excitation energy ΔE. In this case, the Seebeck coefficient S can be expressed by

$$S = \frac{k_B}{e}\left(\frac{\Delta E}{k_B T} + \frac{5}{2} + r\right), \quad (5)$$

where r is a temperature-independent parameter described by the formula, $r = (d \ln \tau / d \ln E)_{E=E_F}$ with a relaxation time τ [31]. Since the majority carrier in this compound is the hole, ΔE corresponds to an energy difference between E_F and mobility edge E_V in the hole band. The observed temperature dependence above 250 K can be interpreted qualitatively based on this equation. We compared the observed S with ideal values calculated using Eq. (5) with the ΔE value obtained with the resistivity data. As a result, we found a small quantitative discrepancy between the observed and calculated values. This suggests that the thermoelectric power in the temperature range is affected not only by thermal activation-type band conduction but also somewhat by other mechanisms, e.g., the effect of minority carriers, polarons, or the surviving 2-D VRH regime.

The thermally induced crossover temperature between the 2-D VRH regime and the activation-energy-type regime is consistent for both resistivity and thermoelectric power measurements. In general, studies on polycrystalline samples sometimes lead to a misleading temperature dependence of resistivity of materials owing to external factors such as grain-boundary scattering. However, in this study, we confirmed by two independent measurements that the crossover of the conduction mechanism occurs at almost the same temperature. In particular, thermoelectric power data are much more reliable because they are not sensitive to the effects of grain-boundary scattering compared with resistivity data. Therefore, we concluded that the crossover occurs around 250 K in this compound.

Fig. 11 shows the temperature dependence of magnetic susceptibility of $(CaOH)_{1.14}CoO_2$. A simple Curie–Weiss-like temperature dependence was observed through the entire temperature range measured. No apparent difference was observed in zero-field cooling data and field cooling ones. Since the present compound is electrically insulating, the magnetic data can be analyzed using the following formula:

$$\chi = \chi_0 + \frac{C}{T-\theta}, \quad (6)$$

where χ_0 is a temperature-independent component of the magnetic susceptibility, C is the Curie constant and θ is the Weiss temperature. Applying these data between 30 and 300 K in Eq. (6), we obtained the parameters:

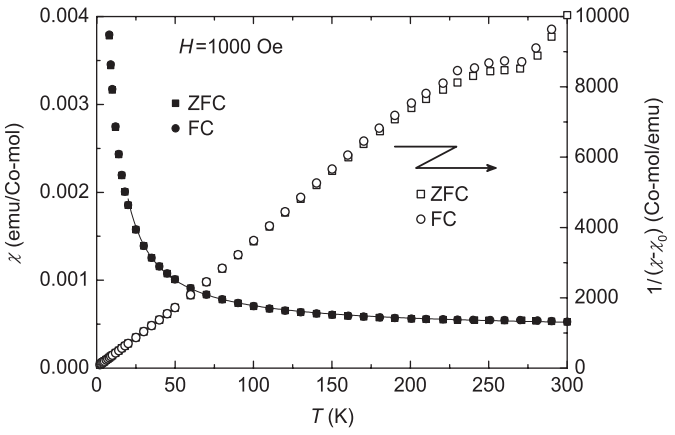

Fig. 11. Temperature dependence of magnetic susceptibility χ per cobalt ion for $(CaOH)_{1.14}CoO_2$. Solid curve shows the result of the fitting with Eq. (6) from 30 to 300 K. The scale of the right vertical axis is for inverse susceptibility $1/(\chi - \chi_0)$, where χ_0 ($= 4.29 \times 10^{-4}$ emu/mol) is a temperature-independent component in the magnetic susceptibility.

$\chi_0 = 4.29(4) \times 10^{-4}$ emu/mol, $C = 0.0278(7)$ emu K/mol, and $\theta = 1.4(7)$ K. The absolute value of θ is very close to zero, suggesting the negligibly weak magnetic interaction between the localized spins. Assuming that the g-factor is 2.0, we estimated the effective number of Bohr magnetons to be 0.471 per cobalt ion. This value is generally comparable with the ideal value of 0.548 expected on the $Co^{2.9+}$ mixed valence state with low-spin configurations, Co^{3+} ($S = 0$, $t_{2g}^6 e_g^0$) and Co^{2+} ($S = 1/2$, $t_{2g}^6 e_g^1$). This suggests that the Curie term originates in the localized electron spins in the cobalt e_g orbital.

Fig. 12 shows a possible electron-band structure estimated from our results. The band structure near the E_F principally consists of a cobalt $3d$ t_{2g} oxygen $2p$ hybridized anti-bonding band ($= t_{2g}$ derivative band) similar to those of the other layer cobalt oxides [40,41]. The t_{2g}-derivative band is the main conduction band, in which holes are doped. However, for the present compound, the t_{2g}-derivative band is estimated to be almost filled, and E_F is placed very close to the band edge. These estimations are consistent with the observed cobalt valence (~3) and the low spin state of cobalt ion. The hole carrier density is extremely small in this situation, which is a rare case of the electronic state for the misfit-layered cobalt oxides.

The carriers in the tail states (hatched area in Fig. 12) cannot move at low temperature because of the localization due to random potential and insufficiency of doped carriers. The hole conduction follows the 2-D VRH regime at low temperature. Near room temperature, some of the holes near E_F are thermally activated to the mobility edge E_V in the t_{2g} band beyond the excitation energy ΔE. This causes the change of the dominant conduction mechanism from the 2-D VRH regime to the semiconductor-like band conduction one. The crossover of these conduction mechanisms appears in both the resistivity and thermoelectric power measurements. We estimated the ΔE ($= E_F$–E_V) value to be about 0.1 eV from the resistivity data.

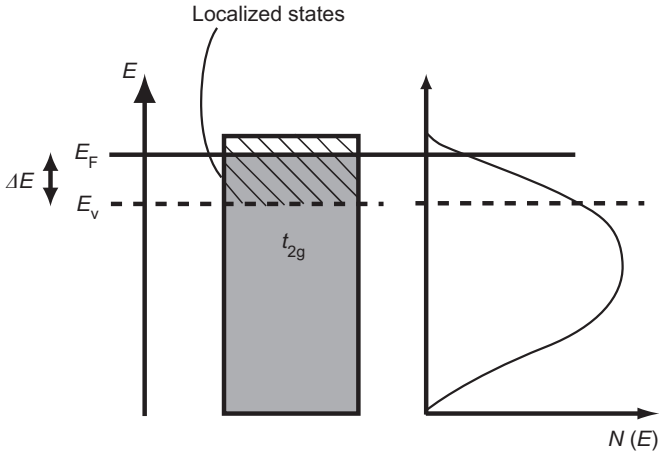

Fig. 12. Electronic-band structure model near Fermi energy level E_F for $(CaOH)_{1.14}CoO_2$. The t_{2g} band crosses the E_F, yielding finite density of states at E_F in the bands. The E_V indicates mobility edge of the t_{2g} band. Hatched area indicates tail states, in which carriers are localized by the random potential.

4. Summary

We succeeded in synthesizing a new layered cobalt oxide $(CaOH)_{1.14}CoO_2$ under high pressure. This compound is a kind of composite crystal consisting of two interpenetrating subsystems: CdI_2-type CoO_2 layers and rock-salt-type $Ca_2(OH)_2$ blocks. The two subsystems have aperiodicity along the a-axis, and are alternately stacked along the c-axis. Hydrogen atoms are situated in the rock-salt-type block as OH^- ions. This compound is the first cobalt oxide that has double rock-salt-type CaOH atomic layers in its structure.

Resistivity and thermoelectric power measurements revealed that the conduction mechanism follows a 2-D variable-range-hopping regime below 220 K, and that it undergoes crossover to activation-energy-type band conduction near room temperature. The positive sign of the Seebeck coefficient clearly indicated that the majority carrier type is the hole throughout the observed temperature range. The crossover of the conduction mechanism seems to be related to thermal excitation of localized holes near the Fermi energy level to the mobility edge in the hole band.

Acknowledgments

We thank Doctors Akaishi, Taniguchi, and Kanke of NIMS for their helpful advice on the high-pressure experiments. One of the authors, M.S., thanks Dr. Sakurai of NIMS for fruitful discussion on synthesis and physical properties. This research work was partly supported by the Superconducting Materials Research Project administrated by the Ministry of Education, Culture, Sports, Science and Technology of Japan.

References

[1] K. Takada, H. Sakurai, E. Takayama-Muromachi, F. Izumi, R.A. Dilanian, T. Sasaki, Nature 422 (2003) 53.
[2] D.J. Singh, Phys. Rev. B 68 (2003) 020503(R).
[3] I. Terasaki, Y. Sasago, K. Uchinokura, Phys. Rev. B 56 (1997) R12685.
[4] A.C. Masset, C. Michel, A. Maignan, M. Hervieu, O. Toulemonde, F. Studer, B. Raveau, J. Hejtmanek, Phys. Rev. B 62 (2000) 166.
[5] R. Funahashi, I. Matsubara, Appl. Phys. Lett. 79 (2001) 362.
[6] T. Yamamoto, K. Uchinokura, I. Tsukada, Phys. Rev. B 65 (2002) 184434.
[7] D. Pelloquin, A. Maignan, S. Hébert, C. Martin, M. Hervieu, C. Michel, L.B. Wang, B. Raveau, Chem. Mater. 14 (2002) 3100.
[8] H. Sakurai, N. Tsujii, E. Takayama-Muromachi, J. Phys. Soc. Japan 73 (2004) 2393.
[9] T. Motohashi, R. Ueda, E. Naujalis, T. Tojo, I. Terasaki, T. Atake, M. Karppinen, H. Yamauchi, Phys. Rev. B 67 (2003) 064406.
[10] J. Sugiyama, J.H. Brewer, E.J. Ansaldo, H. Itahara, T. Tani, M. Mikami, Y. Mori, T. Sasaki, S. Hébert, A. Maignan, Phys. Rev. Lett. 92 (2004) 17602.

[11] E. Takayama-Muromachi, Chem. Mater. 10 (1998) 2686.
[12] H. Yamauchi, M. Karppinen, Supercond. Sci. Technol. 13 (2000) R33.
[13] Y. Miyazaki, M. Onoda, T. Oku, M. Kikuchi, Y. Ishii, Y. Ono, Y. Morii, T. Kajitani, J. Phys. Soc. Japan 71 (2002) 491.
[14] H. Leligny, D. Grebille, O. Pérez, A.C. Masset, M. Hervieu, B. Raveau, Acta Crystallogr. B 56 (2000) 173.
[15] H. Yamauchi, K. Sakai, T. Nagai, Y. Matsui, M. Karppinen, Chem. Mater. 18 (2006) 155.
[16] G. Wiegers, A. Meetsma, S. van Smaalen, R.J. Haange, J. Wulff, T. Zeinstra, J.L. de Boer, S. Kuypers, G. Van Tendeloo, J. van Landuyt, S. Amelinckx, A. Meershaut, P. Rabu, J. Rouxel, Solid State Commun. 70 (1989) 409.
[17] G. Wiegers, A. Meerschaut, J. Alloys Compounds 178 (1992) 351.
[18] S. van Smaalen, A. Meetsma, G.A. Wiegers, J.L. de Boer, Acta Crystallogr. B 47 (1991) 314.
[19] S. van Smaalen, J.L. de Boer, Phys. Rev. B 46 (1992) 2750.
[20] The CaO was prepared from $CaCO_3$ (99.9%) by heat treatment at 1373 K in Ar gas. The $Ca(OH)_2$ was prepared from the CaO powder by reaction with ion-exchanged water. The reacted $Ca(OH)_2$ powder was dried at 473 K before use.
[21] The molar ratio in the starting mixture for the sample corresponds to a nominal composition of $(Ca_{0.98}OH_{0.92})_{1.14}CoO_2$.
[22] Yamamoto, Acta Crystallogr. A 49 (1993) 831.
[23] R.D. Shannon, Acta Crystallogr. A 32 (1976) 751.
[24] We performed the redox-titration experiments for two times, and obtained the cobalt valences 2.93 and 2.94, respectively. The experimental error is estimated to be ± 0.04.
[25] In Fig. 3(c), the [010] direction of the lateral axis is not distinguishable from the [110] direction at glance, because $|2\boldsymbol{b}^*|$ is nearly equal to $|\boldsymbol{a}_1^* + \boldsymbol{b}^*|$ owing to the nearly hexagonal lattice for subsystem-1. If we assign the lateral axis in Fig. 3(c) to the [110] direction, we have to add another possible reflection condition, k, $l = 2n$ for $0\,k\,l\,0$, and further two possible space groups, *Cccm* (no. 66) and *Ccc*2 (no. 37), of the fundamental structures for the two subsystems. However, these space groups cannot generate a plausible crystal structure model. We therefore removed the *Cccm* (no. 66) and *Ccc*2 (no. 37) from the candidates for the actual space group realized in the present compounds. Anyway, regardless of choice of the direction, [010] or [110], the possible space groups are limited to *Cmcm* (no. 63), $Cmc2_1$ (no. 36), and *C*2*cm* (no. 40).
[26] S. Lambert, H. Leligny, D. Grebille, J. Solid State Chem. 160 (2001) 322.
[27] From this simulation, we confirmed that the strong preferred orientation exists in the XRD pattern. In Fig. 2, the intensities of 0 0 8 0, 0 0 *10* 0, and 0 0 *12* 0 lines look rather small at glance; however, they are also enhanced as good as the 0 0 2 0, 0 0 4 0, and 0 0 6 0 lines at lower angles. Because of this strong preferred orientation, we could not reproduce perfectly the intensities of all reflections, especially for 0 0 8 0 (~41.8°) and 0 0 *10* 0 (~53.0°) reflections in Fig. 7.
[28] R.W.T. Wilkins, A. Mateen, G.W. West, Am. Miner. 59 (1974) 811.
[29] S.R. Shieh, T.S. Duffy, Phys. Rev. B 66 (2002) 134301.
[30] K. Takada, M. Osada, F. Izumi, H. Sakurai, E. Takayama-Muromachi, T. Sasaki, Chem. Mater. 17 (2005) 2034.
[31] N.F. Mott, E.A. Davis, Electronic Processes in Non-crystalline Materials, second ed, Clarendon Press, Oxford University Press, Oxford, 1979 (Chapter 2).
[32] E.M. Hamilton, Philos. Mag. 26 (1972) 1043.
[33] A.L. Efros, B.I. Shklovskii, J. Phys. C 8 (1975) L49.
[34] Below about 80 K, resistivity increase rapidly strays out of any conduction mechanisms. We conceive that this is not intrinsic property of the present phase and is due to the problems of the measurement system on measuring the high-resistance sample. In this paper, we do not discuss the resistivity data in the temperature range.
[35] T.H. Geballe, G.W. Hull, Phys. Rev. 98 (1955) 940.
[36] I.P. Zvyagin, Phys. Stat. Sol. B 58 (1973) 443.
[37] V.V. Kosarev, Sov. Phys. Semicond. 8 (1975) 897.
[38] H. Overhof, Phys. Stat. Sol. B 67 (1975) 709.
[39] W. Brenig, G.H. Döhler, P. Wölfle, Z. Phys. 258 (1973) 381.
[40] T. Takeuchi, T. Kondo, T. Takami, H. Takahashi, H. Ikuta, U. Mizutani, K. Soda, R. Funahashi, M. Shikano, M. Mikami, S. Tsuda, T. Yokoya, S. Shin, T. Muro, Phys. Rev. B 69 (2004) 125410.
[41] D.J. Singh, Phys. Rev. B 61 (2000) 13397.